Residual stresses and microstructure in Powder Bed Direct Laser Deposition (PB DLD) samples

X. Song · M. Xie · F. Hofmann · T. Illston · T. Connolley ·
C. Reinhard · R. C. Atwood · L. Connor ·
M. Drakopoulos · L. Frampton · A. M. Korsunsky

Abstract In the present study, residual stresses in the Powder Bed Direct Laser Deposition (PB DLD) built parts were investigated using X-ray diffraction strain measurement and finite element simulation. The microstructure and texture of the DLD built parts were studied, indicating that the vertically elongated grains have preferred orientation of (001)-type pointing in the growth direction in the nickel superalloy C263. A conceptual model of residual stress generation was proposed using fictitious thermal expansion based on the argument that residual stresses arise from strain incompatibility that is "frozen in" within the work piece during fabrication.

X. Song (✉)
Singapore Institute of Manufacturing Technology, A* Star,
Singapore 638075, Singapore
e-mail: xsong@simtech.a-star.edu.sg

M. Xie · F. Hofmann · A. M. Korsunsky
Department of Engineering Science, University of Oxford, Parks Road, Oxford, UK OX1 3PJ

T. Connolley · C. Reinhard · R. C. Atwood · L. Connor ·
M. Drakopoulos
Diamond Light Source, Beamline I12 JEEP, Didcot, Oxon, UK OX11 0DE

L. Frampton
Materials Application – Engineering, ELT-17, Rolls Royce Plc,
Derby, UK DE24 8BJ

T. Illston
Materials Solutions, Great Western Business Park, McKenzie Way,
Worcester, UK WR4 9GN

Introduction

Powder Bed Direct Laser Deposition (PB DLD) is a type of additive manufacturing technique [1] that uses high power laser beams to fuse small particles of plastic, metal, ceramic, or glass powders into a mass that has a desired 3-dimensional shape. The laser selectively fuses powdered material by rastering cross-sections generated from a 3-D digital description of the part on the surface of a powder bed. After each cross-section is scanned, the powder bed is lowered by one layer thickness, a new layer of material is applied on top, and the process is repeated until the part is completed. It is sometimes also referred to as Selective Laser Sintering (SLS) or Selective Laser Melting (SLM). When this method is applied to metal powder, it is usually denominated Direct Metal Laser Sintering (DMLS). The procedure and equipment used in the present study were developed by EOS (Munich, Germany) [2]. It is worth noting that this method is different from laser cladding [3] since laser cladding requires "live" feedstock material (either in powder or wire form) to be fed in to the system locally, rather than selectively using uniform powder layers in a sequence.

The earliest applications of the Direct Laser Deposition (DLD) technique have been on the toolroom end of the manufacturing spectrum. DLD can drastically reduce the manufacturing lead time and cost of developing prototypes of new parts and devices, previously achieved by subtractive methods which are typically slow and expensive. As additive manufacturing technologies develop and mature, DLD is moving further towards the production end of manufacturing activities. Additive manufacturing provides an extremely flexible, yet competitive and economically viable, method which appears well-suited to the manufacture of aero-engine combustion components with complex shapes. For such components the manufacturing cost using a subtractive method would be high or prohibitive. Examples of such components

used in combustion systems include swirlers, fuel injectors, and cooling tiles. However, the DLD process is also known to introduce large residual stresses [4]. These are sometimes so large that they cause cracking in the sample even before it can be removed from the base platen for post-DLD heat treatment.

Numerous FE simulation studies of the DLD process have been carried out in recent years [5–7] with attempts to capture the temperature and stress evolution during the process. Some studies even took into consideration the phase transformation [8] and liquid flow [9] effects. Reasonably good agreement between numerical simulation and experimental results has been reported [5–9]. Practical suggestions have been made for residual stress reduction [10]. However, as numerical models are developed to achieve a better match with reality, they inevitably become three dimensional and very complicated [11–13]; so that it may take much longer time to run the model than the actual process. This makes the simulation of the DLD fabrication of a real complex engineering component nearly impossible. Therefore, some form of simplification has to be made in the simulation to assist in understanding the origins and sources of residual stresses. One common practice is to simplify the process by ignoring the scanning strategy. This method considers, rather than each individual scanning pass, scanning layer as the basic "building block" for simulation [14]. However, there exists the alternative that, by simplifying the component geometry, normally from 3D to 2D, each individual scanning pass can be simulated, as in this case each pass represents one layer. Here we adopt the second approach to seek a simplified "first order approximation" to allow the evaluation of residual stresses in DLD work pieces, as it allows direct comparison with experimental evaluation of strain and stress using high energy synchrotron X-ray diffraction, which the first approach cannot achieve. Therefore, we employ a 2D thermo-mechanical fully-coupled finite element model for the simulation of the 2D problem: building a single DLD bead on the top surface of a tool steel base plate

Description of the material and process

The laser-sintering system used in the present study was an EOSINT M 270 [2]. The baseplate was made from standard ferritic tool steel and the part was to be sintered from fine-grained C263 Nickel superalloy powder. Within the operation range of the machine, the IPG fibre laser was used with a power of 195 W, scan speed of 900 mm/s, and scan spacing of 0.08 mm. A laser spot of 100 μm was used, and each new powder layer was 20 μm in thickness. Multiple parallel single lines of different heights were made, with the spacing of 10 mm. It is hoped that this relatively large spacing (compared to the 100 μm wall thickness) ensures that mutual influence between walls is minimized. To investigate the influence of the scan line height, 20 μm, 40 μm, 80 μm, 160 μm, 320 μm,

640 μm, 1 mm, 2 mm, 4 mm and 8 mm high thin DLD walls were built. The length of each wall was set to 100 mm. Plane strain conditions were assumed along the scan direction, and plane stress condition in the transverse direction. Figure 1 shows the configuration of the multiple parallel lines. The design of the test specimen was chosen to match the 2D numerical simulation approach adopted in the present study. Such 2D experimental configuration was also chosen by other researchers [15] to be the setup of the DLD microstructure study.

Collecting information on the thermal history of the parts during the DLD built-up process was not possible due to the difficulty of access to the processing chamber. It was, however, known from the technical specification that the melt pool cools down to close to room temperature in microseconds, and that the baseplate temperature does not increase above the threshold of 80 °C. It is then possible to draw the conclusion that no gradual built-up of heat occurred in the sample during processing. Rather, the melt pool cooled rapidly due to its small size, with the principal direction of the heat flux being vertically downwards through the sample to the Base plate.

Microstructure and grain orientation

The microstructure of the samples consists of elongated grains that grow in the direction of material build-up during deposition, with the grains extending across several individual deposition layers. Micrographs shown in Fig. 2a and b were collected from DLD-built parts with the same processing parameters. In the horizontal cross-sectional plane (perpendicular to the grain growth direction), equiaxial grain structure shown in Fig. 2a is observed. On the other hand, in the vertical section plane shown in Fig. 2b, grains appear elongated in the direction of growth. This type of grain morphology, in combination with the mechanical anisotropy of FCC nickel alloys indicates that the mechanical properties of the produced polycrystalline parts, such as stiffness and strength, are expected to vary depending on the direction of loading. The directional grain growth mechanism has been well explained metallurgically in Gaumann's work [16] and observed in laser rapid prototyping of many Ni-based superalloys [15, 17, 18].

The significance of the microstructural observations for residual stress analysis is that the temperature gradients that develop in the workpiece are dominatingly unidirectional in nature, making the orientations transverse to the material build-up largely equivalent. It is therefore concluded that (i) the vertical temperature gradient acts as the principal source of strain mismatch, and (ii) that qualitatively the residual stress state can be well understood using simple 2D modelling.

Figures 3 and 4 show EBSD results from the transverse and longitudinal sections through the samples, respectively. From these observations, especially Fig. 3b and c, it is clear that

Fig. 1 **a** Transverse and **b** Longitudinal view of DLD "walls" of different heights
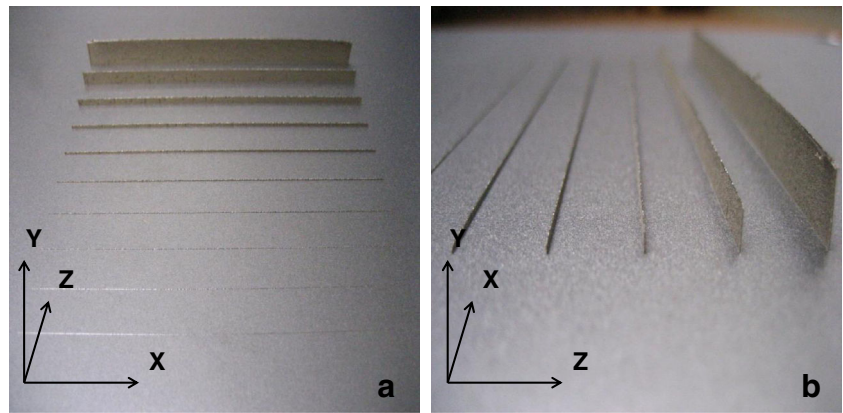
elongated grains have preferred orientation, with the (001)-type normals pointing in the growth direction (i.e. vertically). This finding coincides with that of Moat [19], Dinda [15] and Zhao [17] and further confirms that Gaumann's grain growth mechanism is likely to be active [16]. This assumption can be incorporated into the simplified 2D numerical model of DLD process, to allow the prediction of microstructure evolution during direct metal laser sintering.

Finite element modelling

Modelling a moving heat source

The physical phenomenon associated with the interaction of the laser and the melting pool is complex. A number of models are available to describe the heat source that represents laser heat input. Goldak's [20, 21] ellipsoidal heat source model used here has been widely employed in the literature [22]. This model takes into account the heat transported below the focus plane when the additional material is deposited. The ellipsoidal temperature distribution is described using the non-dimensional effective radius, R_e, i.e. the re-normalised distance from the laser spot centre, (x_0, y_0, z_0)

$$R_e = \sqrt{A(z-z_0)^2 + B(x-x_0)^2 + C(y-y_0)^2}. \tag{1}$$

The volumetric heat input, q, varies spatially as a function of this effective radius from the centre of the laser position, according to the function

$$q(x,y,z) = q_{max} e^{-R_e^2}. \tag{2}$$

In Eq. (1), x_0, y_0 and z_0 give the laser beam centre position relative to the Cartesian axes, and x, y and z represent the position where the heat flux is evaluated. Assuming an ellipsoid centred at (x_0, y_0, z_0) with semi-axes a, $\underline{b}$, and c, the constants A, B and C in Eq. (1) may be evaluated by assuming (as in [20]) that the heat flux decays to 5 % of the maximum value at the ellipse boundaries. The shape of the simulated heat flux is similar to that for the Tungsten Inert Gas (TIG) welding process [23]. Hence, a is taken to be the distance from the laser bead start point to the centre, and b is the half bead width, and c the bead height. Following the analysis in [20],

$$R_e = \sqrt{3\left(\frac{z-z_0}{a}\right)^2 + 3\left(\frac{x-x_0}{b}\right)^2 + 3\left(\frac{y-y_0}{c}\right)^2} \tag{3}$$

Substituting (3) into (2), the expression for the weld torch heat flux, q, as a function of position (x, y, z) is obtained,

$$q(x,y,z) = q_{max} e^{-3\left(\frac{z-z_0}{a}\right)^2 - 3\left(\frac{x-x_0}{b}\right)^2 - 3\left(\frac{y-y_0}{c}\right)^2}. \tag{4}$$

Fig. 2 Microstructure of the DLD thin wall (etched electrolytically using Nimonic etchant): **a** transverse section at ×100 magnification; **b** longitudinal section at ×50 magnification (the vertical build orientation is shown horizontally across the page) [34]
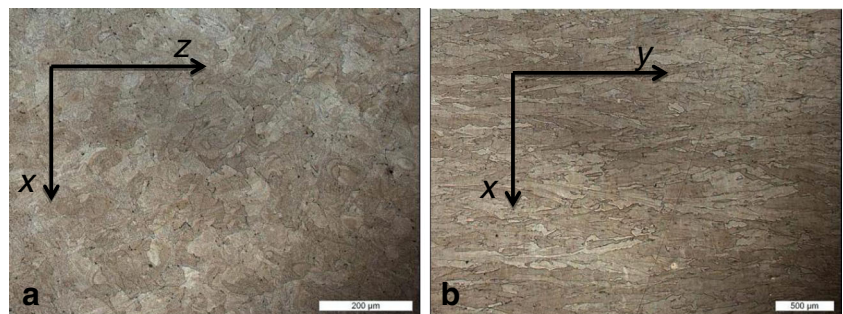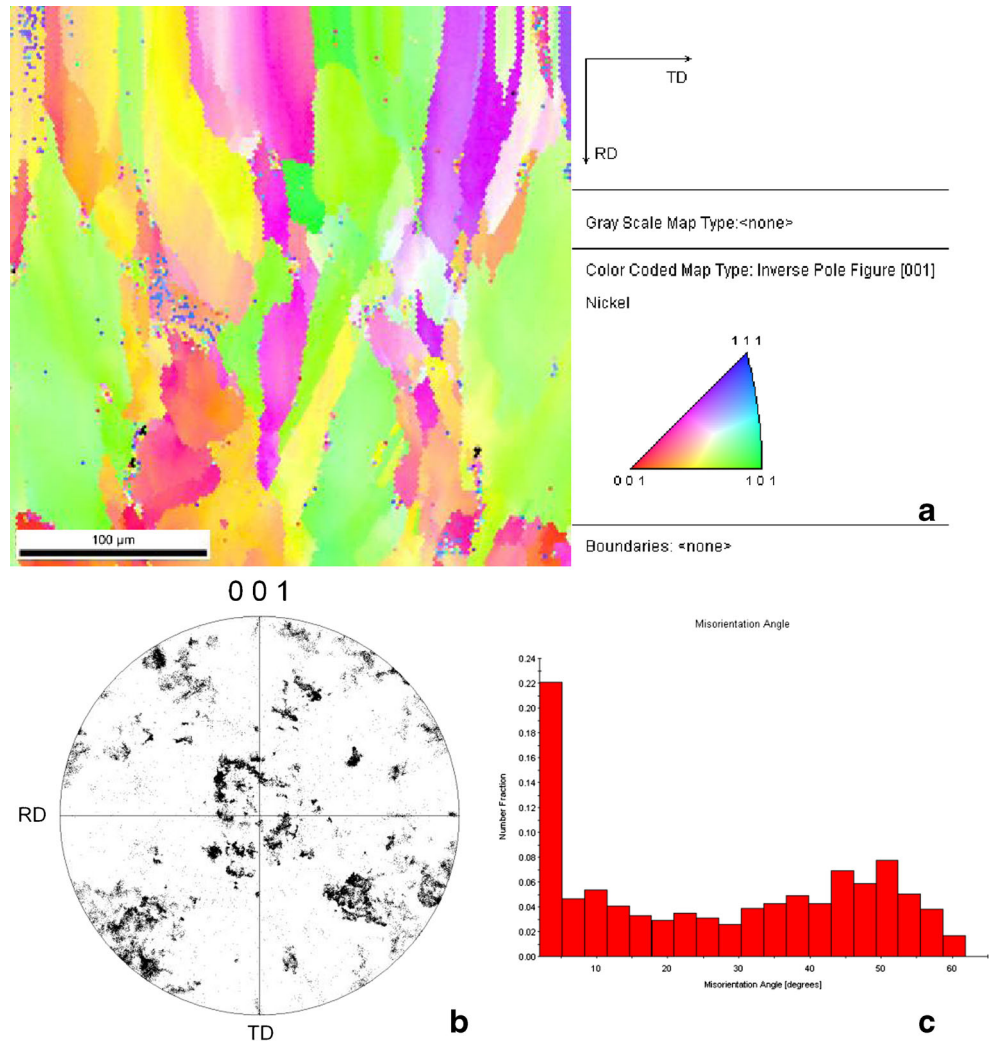
Fig. 3 EBSD result from the transverse section of the sample (see Fig. 7a): **a** the basic crystallographic triangle showing the grain orientation colour map; **b** pole figure of the sample showing the grain orientation distribution; **c** misorientation angle distribution (in degrees, range 0° to 65°) with respect to the (001) direction

The heat input at different positions of the bead depends on the position of the laser spot as it travels along the centreline with speed v. The current position can be calculated as a function of the process time, t. Equation (4) can then be generalised to account for the moving laser spot as,

$$q(x, y, z) = q_{max} e^{-3\left(\frac{z - z_0 - vt}{a}\right)^2 - 3\left(\frac{x - x_0}{b}\right)^2 - 3\left(\frac{y - y_0}{c}\right)^2} - q_i \qquad (5)$$

The peak heat flux, q_{max}, is obtained by integrating the volumetric heat flux distribution (5) over the entire body and equating it to the total heat input to give,

$$q_{max} = \frac{6\sqrt{3}Q}{\pi^{3/2}(abc)} \qquad (6)$$

In Eq. (6), Q is the energy input rate (J/s) which is given by the product of the heat input (J/mm), laser speed (mm/s) and the laser efficiency. Note that laser efficiency of unity was

assumed, i.e. all the heat generated by the weld torch was transmitted to the plate and weld metal. In Eq. (5), q_i is included to account for heating conduction away from the weld spot through the DLD part. The value of q_i is given by

$$q_i = c_p \rho_w \Delta T \frac{v}{S} \qquad (7)$$

where c_p is the specific heat capacity of the material, ρ_w is the density of the DLD part, ΔT is the temperature difference, v is the speed of the moving heat source, and S is the DLD bead length. Although the specific heat capacity depends to a certain extent on the temperature, for simplicity the value of c_p used was the value at the melting temperature. The user subroutine DFLUX in ABAQUS [24] was used to introduce the body flux described by Eq. (5). The subroutine first calculates the position of the laser spot according to the process time, t, and then computes the heat flux, q, at each

Fig. 4 EBSD result from the longitudinal section sample (see Fig. 7b): **a** the basic crystallographic triangle showing the grain orientation colour map; **b** pole figure of the sample showing the grain orientation distribution; **c** misorientation angle distribution (in degrees, range 0° to 65°) with respect to the (001) direction
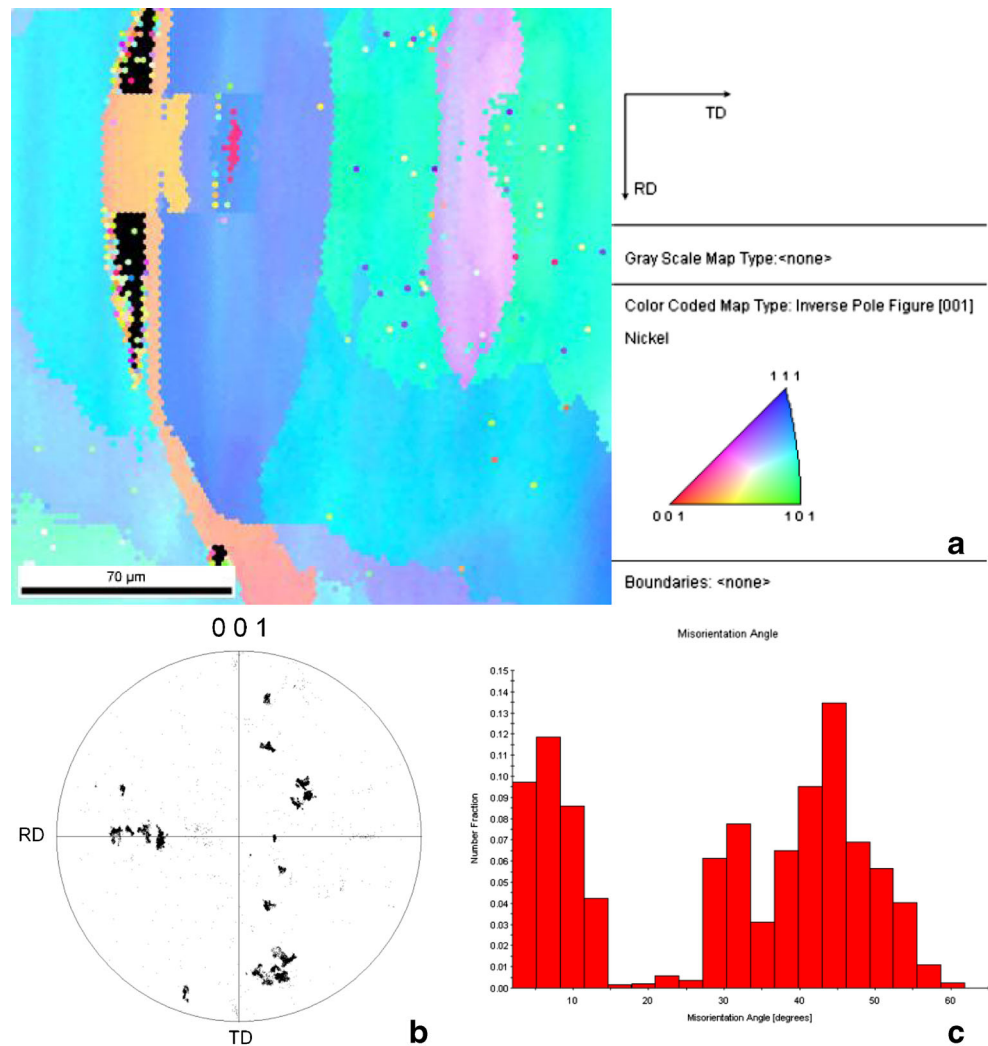

Integration Point (IP). As the model was 2D in nature with plane strain thickness of unit length, the heat flux was first calculated in 3D, then integrated and averaged through the unit length and assign to the corresponding IP in the 2D model in the subroutine. Therefore, in this approach, only one fictional unit length 3D element has to be computed in each layer, with consideration of heat source approaching and leaving the element using a threshold value. This helps to reduce the computation time significantly in 2D model configuration. However, the time interval between each layer has to be pre-calculated based on the actual scanning pass length and travel speed so that the model can be built up layer by layer in an incremental manner at the right step time.

Material properties

The material thermo-mechanical properties used in the model were taken from the literature [25, 26] and listed in the model as tables for thermal conductivity, thermal expansion, special heat, Young's modulus and plasticity. They are temperature-dependent properties up to the melting temperature of 1257 °C and 1400 °C for C263 and 316 L, respectively. Latent heat for C263 (as melting only happens in C263) is set to be 297 J/kg · °C, with solidus temperature of 1257 °C and liquidus temperature of 1369 °C. Heat loss by the weld pool also occurs due to radiation and convection, especially at high temperature. Radiation and convection heat losses were modelled in ABAQUS using the *RADIATION and *FILM options. The radiation coefficient (emissivity) and convection coefficient were assumed to be independent of the temperature. When the DLD built part is growing, new surface becomes available for radiation and convection, and this is taken into account in the analysis. The entire model was encastred at a corner node to constrain its spatial Degree-Of-Freedom (DOF). The initial temperature was set to be ambient temperature of 25 °C. To account for the effects of material melting and re-solidification and annealing, the ABAQUS command *ANNEAL TEMPERATURE was used. This command causes a point in the material to lose its hardening history by setting the equivalent plastic strain at that point to zero, providing a

Fig. 5 Definition of the coordinate system, and the configuration of the 2D DLD FE model
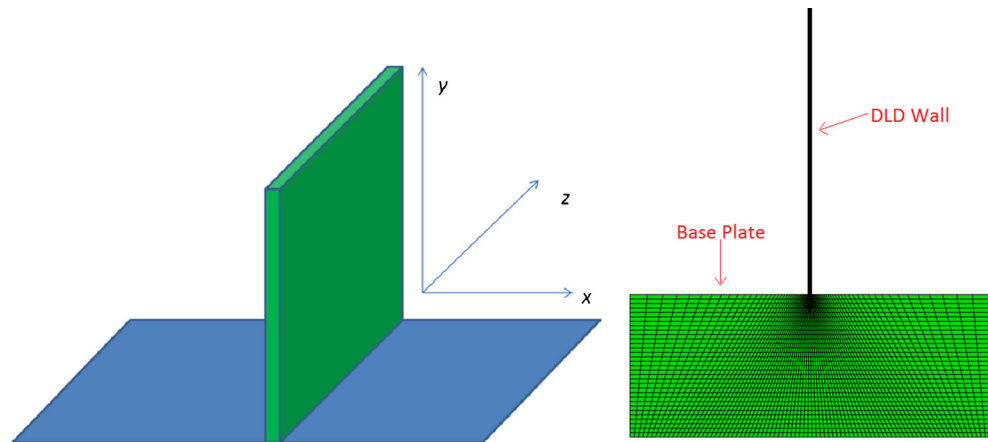
certain threshold temperature is exceeded. An isotropic hardening model can overestimate the residual stress, should cyclic hardening occur, whereas a kinematic hardening assumption may underestimate it. Therefore, a combined kinematic/isotropic model was employed to represent accurately the material behaviour.

Solution strategy

To reflect the additive nature of the process, a finite element simulation technique called "element birth (and death)" [27] was employed, together with moving heat source description in subroutine DFLUX. In this approach, sections of the DLD part elements were added incrementally and individually to represent the incremental nature of the DLD metal deposition process. The stages of the analysis were as follows. Stage 1: initially all bead elements were de-activated (element death). Stage 2: sections of the DLD bead were re-activated (element birth) in successive steps to simulate DLD metal deposition as the laser spot travelled along the plate. Stage 3: one DLD deposition was completed, the plate was allowed to return to steady state temperature (room temperature). In this work the steady state was defined as the time at which the temperature

change per unit time everywhere in the DLD part was less than 0.001 °C/s. In Stages 1 and 2, the *MODEL CHANGE option in ABAQUS was used to add and remove the DLD bead elements. The length of the DLD bead element sections added in each step was related to the size of the ellipsoidal heat flux distribution and the laser scan velocity in the vertical direction.

The approaches of the type described above have been used previously to carry out 3D simulations of laser deposition. However, the model used in the present study was 2D rather than 3D. This analytical approach was adopted because during laser scanning in the longitudinal direction with respect to the wall being built up, the plane strain condition remains valid in the cross section perpendicular to the wall extension. Furthermore, the high energy synchrotron X-ray diffraction measurements conducted to validate the simulation that are described in the next section provided spatial resolution in the direction perpendicular to the beam, but not along the beam, due to the shape of the sampling volume.

The 2D model chosen represented ANY cross section perpendicular to the laser scanning direction, with the nominal thickness of 1 μm used. Comparing to the laser spot size of approximately 100 μm, constant heat influx through the
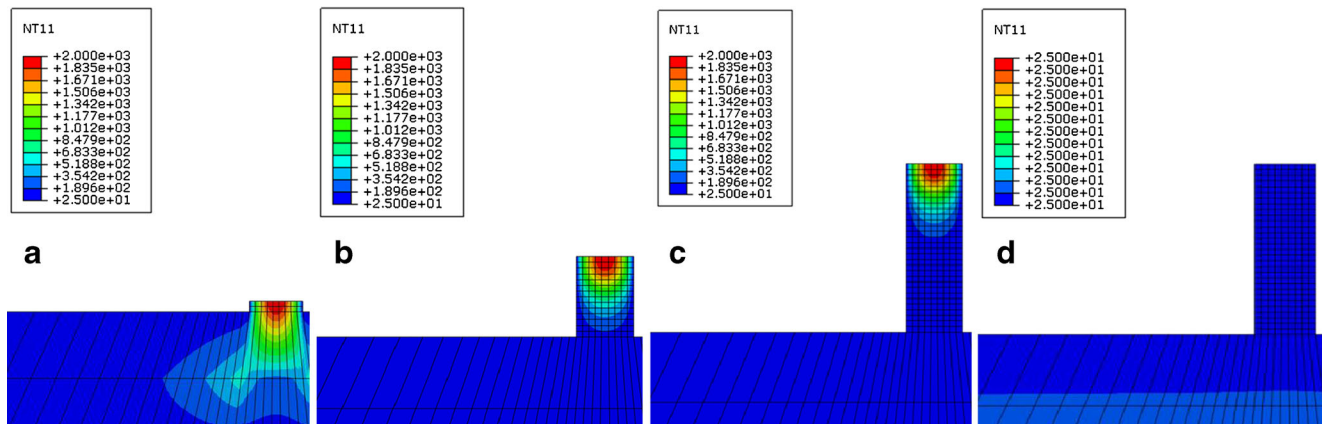

Fig. 6 Temperature evolution history (in °C) for DLD layers: **a** 1st, **b** 7th; **c** 15th; **d** 15th layer in equilibrium state
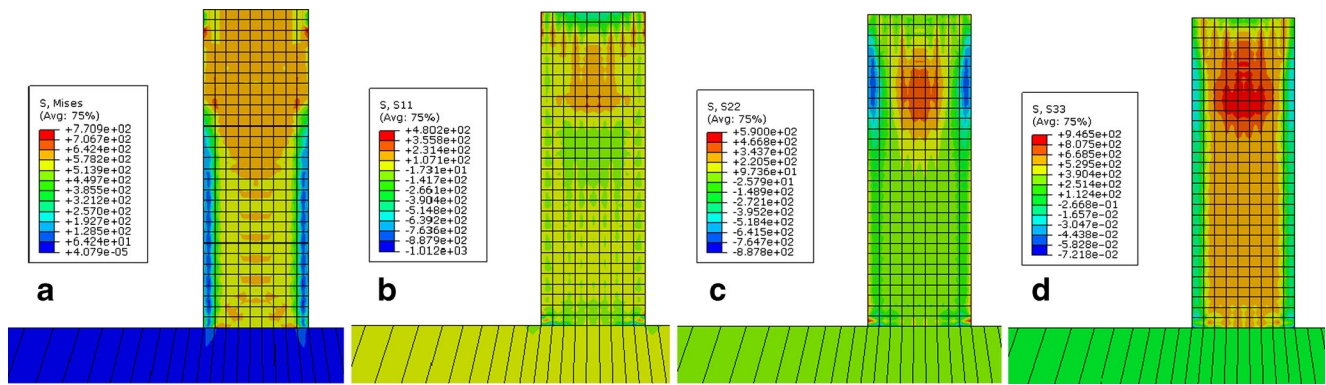
Fig. 7 Contour of the **a** Von Mises **b** x-axis **c** y-axis **d** z-axis residual stresses (MPa) in the DLD part and base plate

thickness could be assumed, and hence the heat source described above in 3D was reduced (projected) into 2D. The element type was chosen to be quadratic CPE8T, the size of which was set to be 10 μm (H)×10 μm (V). Therefore, for each DLD built layer, 10 (H)×2 (V) quadratic elements were added to the model, corresponding to 20 μm incremental layer thickness. The model was built to accommodate the highest DLD wall of 8 mm, with 5 mm of substrate on each side (given the spacing between the walls of 10 mm). Figure 5 gives the model setup configuration. Fully-coupled thermal-mechanical procedure was employed in the simulation.

Results and discussion

Thermal history

Figure 6 illustrates the temperature field at different stages of the DLD process. Figure 6a is in the middle of the first step when the first DLD layer is being built, the laser heat source passing through the cross section. Figure 6b and c correspond to the middle of the 7th and 15th layers respectively. Figure 6d is at the end of the 15th step when equilibrium is established. The temperature field in Fig. 6a-c appears close to

experimental conditions: the size of the area where temperature is close to the melting point corresponds to 80 μm, equal to the lateral spacing between laser scan passes in the experiment and indicating the dimension of the re-solidification area. Comparing Fig. 6c and d confirms that in the model, the temperature drops to RT within 1 ms as observed in the experiment, and that the base plate temperature never exceeds 80 °C.

Residual stresses profile

Figure 7 illustrates the residual stress profile in the DLD built part and base plate. It is worth noting that, from Fig. 7a, the Von Mises residual stresses in the base plate do not exceed 70 MPa, which is relatively small comparing to those in the DLD built part. This is due to the fact that the DLD built part is a thin wall structure compared to the massive base plate. Hence, stress balance suggests that the residual stresses caused by it are relatively small within the base plate. Such claim is confirmed by a quick parametrical study on the influence of the element size for the base plate has been added in the current revision (Fig. 8). It demonstrates that the element size (element aspect ratios are 1:10, 1:1 and 1:0.5 for Fig. 8a, b and c, respectively.) play a minor role in the distribution of the
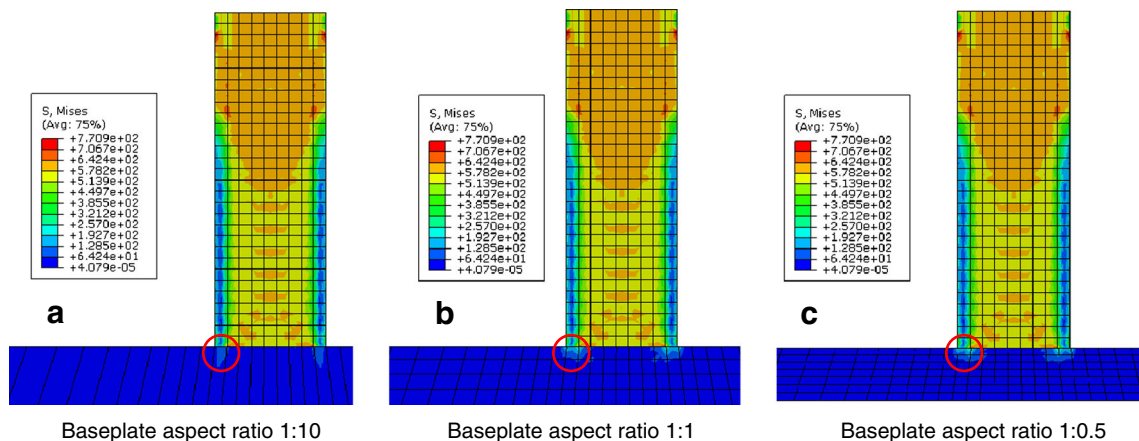

| Baseplate aspect ratio 1:10 | Baseplate aspect ratio 1:1 | Baseplate aspect ratio 1:0.5 |

Fig. 8 Baseplate simulation element size sensitivity study: element aspect ratio **a)** 1:10, **b)** 1:1 and **c)** 1:0.5
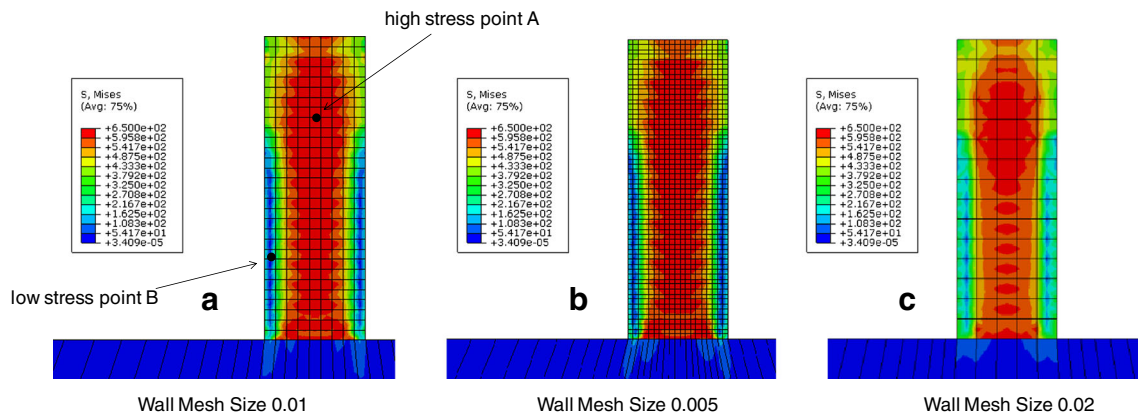
Fig. 9 Element size sensitivity study for the top wall: **a** mesh size 0.01 mm; **b** mesh size 0.005 mm; **c** mesh size 0.02 mm

residual stresses in the base plate. It neither affects the maximum residual stress value (64 MPa) in the baseplate, nor its location, which is in the two corners of the wall/plate interface, and it is not sensitive to the mesh (as it is in the corner).

Another important feature worth noting is that the stresses on the edges of the wall are close to zero as they are the "free" edges, but the stresses build up in the centre of the wall to relatively high values ~500 MPa. Hence, significant stress gradients may exist between the core of DLD component and its edges. The stress in the top (last built) layer is even higher, especially the stress along the wall thickness direction (z-axis). Maximum residual stress can go up to 946.5 MPa (Fig. 7d), which is over C263 material's yield stress and close to that of its ultimate tensile stress at room temperature, making it potentially prone to cracking (Fracture Mode I: opening along the wall), as observed for the 8 mm-high DLD wall in the experiment (Fig. 1b).

A parametrical study on the influence of the element size for the wall has also been carried out. Figure 9 illustrates the residual stress distribution of the wall for different element sizes of 0.01, 0.005 and 0.02 mm (Fig. 9a, b and c). It demonstrates that the distribution of the residual stresses, though very similar, differ more for some than others. The pattern of the residual stress distribution resembles to a continuous pinetree shape in fine mesh of 0.01 and 0.005 mm, but broken in coarse mesh 0.02 mm. This indicates that the
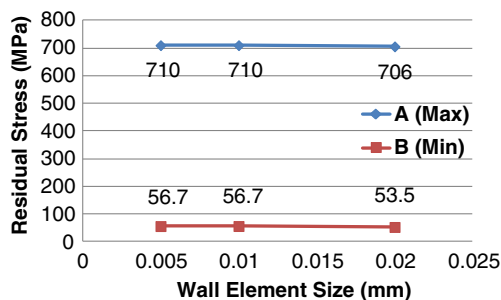
convergence is at 0.01 mm with two elements in vertical direction for one layer increment (each layer is a pinetree branch). Therefore, 0.01 mm is our current selection of the mesh size for the DLD wall structure. If only the highest and lowest stress positions are spotted in the model, their values don't fluctuate much with the mesh element size, maximum value slightly drops from 710 MPa for 0.005 mm and 0.01 mm to 706 MPa for 0.02 mm and minimum value (except surface points) also drops from 56.7 MPa for 0.005 mm and 0.01 mm to 53.5 MPa mm for 0.02 (Fig. 10).

A simplified conceptual thermal expansion model for quick evaluation of residual stresses

For rapid residual stress evaluation in DLD built parts, a conceptual thermal contraction model is proposed here based on the 2D assumption. We argue that the residual stress in the DLD parts at the interface is mainly caused by the difference in temperature and deformation state of the metal already deposited, and the new material being added in the liquid or partially softened form. Thermal expansion coefficient mismatch between the DLD part material and the base plate is a significant initial effect that has to be taken into account. During the subsequent DLD process, the powder is brought up to the temperature exceeding its melting point. While it is in liquid form, no residual stresses are developed. When the material cools down from melting point to the room temperature (in ~1 ms), internal stresses and incompatibilities develop, re-balance and persist thereafter.

In order to test ideas, a simple thermal contraction model was implemented of a DLD wall (see Fig. 11, the y-z plane of the wall viewed along the x axis). The residual stresses in the model were developed through introducing strain incompatibility between the DLD thin wall and the base plate by temperature change from melt temperature to RT. Both the wall and base plate shrink, but do so at a different rate, due to the difference in the thermal expansion coefficients and residual stresses develop. Plane stress assumption was used.

Fig. 10 Change in the maximum and minimum residual stresses value in the wall due to different element sizes

Fig. 11 Thermal contraction model (**a**) setup with boundary conditions and (**b**) residual elastic strain in horizontal direction developed in the entire DLD wall of height 8 mm and length 50 mm (base plate is not shown)
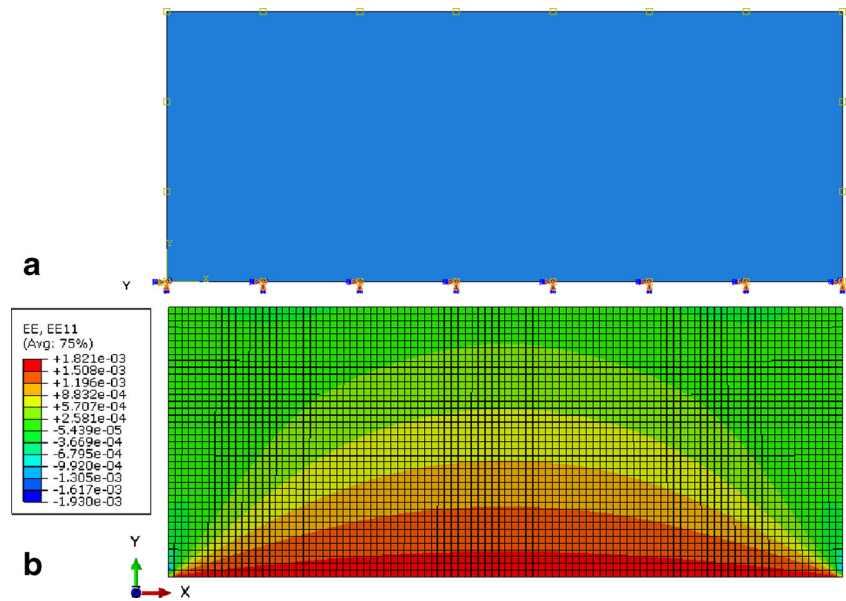
The model was validated through x-ray diffraction experiment of residual stress measurement. X-ray diffraction method has been employed for the measurement of residual stresses in the metallic components for decades [28]. The laser processing components have also been studies recently using X-ray [29], either using lab-based equipment [30] on the sample surface or synchrotron X-ray [30] in the bulk thanks to its high energy penetration and parallelity. The current experiment was carried out using synchrotron X-ray diffraction on beamline I12 JEEP at the Diamond Light Source (Oxfordshire, UK). A monochromatic 2-D diffraction setup was used to collect diffraction patterns. The incident beam had the photon energy of 84.7525 keV and was collimated to the spot size of 0.1×0.1 mm^2. The beam penetrated through the entire thickness of the sample, and scattered away to form a set of diffraction cones. A cross-section through this set of cones was recorded by the two-dimensional detector MAR345 with the pixel matrix of 2880(H)×2881(V) and pixel size of 150 μm. The diffraction patterns (Debye–Scherrer rings) registered by the detector were analysed using Fit2D via the procedures of "caking" and binning to obtain the equivalent 1-D profiles [31, 32]. Then Rietveld refinement [33] was carried out on the binned 1-D diffraction patterns using GSAS (General Structure Analysis System) software to determine the apparent value of the lattice parameter within each gauge volume. The entire thin wall section was scanned and residual strains were calculated based on the stress-free lattice parameter obtained at the sample top left corner.

Figure 12a and b plot the horizontal strain component (ε_{zz}, also denoted EE11 within the FE model) along the horizontal line at $y=0.5$ mm and the vertical line at $z=1$ mm. Plots clearly show that the model prediction has captured the experiment results reasonably well in terms of both magnitude and trend. This model has the potential to be used for rapid evaluation of the residual stresses in complex shape DLD samples. By implementing a temperature change, incompatible strain (eigenstrain) can be introduced as the source of residual stresses development, and can serve to obtain an initial educated guess of the actual stress value in DLD parts.
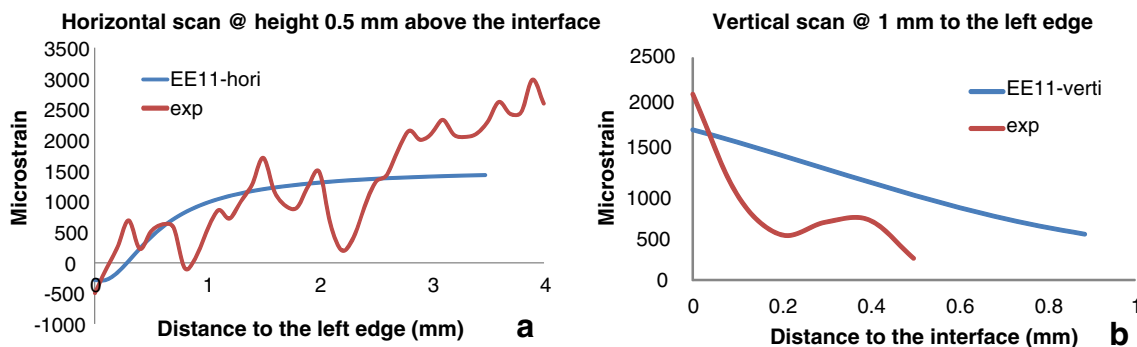

Fig. 12 Comparison of residual strain profiles (horizontal component) between the model and experiment: **a** along a *horizontal line* at height of $y=0.5$ mm above the interface; **b** along a *vertical line* at $z=1$ mm from the left edge

Conclusions

DLD-built parts were investigated using finite element process simulation and X-ray diffraction strain measurement. From the simulation results and experimental data, especially from the simplified conceptual thermal expansion model, it was argued that the process of residual stress creation can be understood based on the consideration of the thermal strain incompatibility with the base plate, and the consideration of thermal gradients in the built part itself. The approach needs to be taken further by simulating the incremental addition of new eigenstrain-containing volumes of material to the model in a piece-wise fashion, as the laser deposition proceeds. This incremental inverse eigenstrain method has the potential to simplify further process simulation, and can provide useful analytical tools for the understanding of the DLD process.

References

1. ASTM (1994) Standard terminology for additive manufacturing technologies, ASTM International document F2792-10, West Conshohocken, PA
2. EOS GmbH: http://www.eos.info/en/products/systems-equipment/metal-laser-sintering-systems.html, Krailling, Germany
3. Vilar R (1999) Laser cladding. J Laser Appl 11:64–79
4. Lyon S, Frampton L (2010) Statement of work for the optimisation of Powder Bed Direct Laser Deposition (PB DLD) in C263. RR Internal Report, MFR47541, Issue 2
5. Dai K, Shaw L (2004) Thermal and mechanical finite element modeling of laser forming from metal and ceramic powders. Acta Mater 52:69–80
6. Dai K, Shaw L (2006) Parametric studies of multi-material laser densification. Mater Sci Eng, A 430:221–229
7. Dai K, Shaw L (2001) Thermal and stress modelling of multi-material laser processing. Acta Mater 49:4171–4181
8. Ghosh S, Choi J (2006) Modelling and experimental verification of transient/residual stresses and microstructure formation in multi-layer laser aided DMD process. J Heat Trans-T ASME 128:662–679
9. Chen TB, Zhang YW (2006) Three-dimensional modelling of selective laser sintering of two-component metal powder layers. J Manu Sci Eng-T ASME 128:299–306
10. Matsumoto M, Shiomi M, Osakada K, Abe F (2002) Finite element analysis of single layer forming on metallic powder bed in rapid prototyping by selective laser processing. Int J Mach Tool Manu 42:61–67
11. Wang L, Felicelli S, Gooroochurn Y, Wang PT, Horstemeyer MF (2008) Optimization of the lens process for steady molten pool size. Mater Sci Eng, A 474:148–156
12. Zaeh MF, Lutzmann S (2010) Modelling and simulation of electron beam melting. Pro Enging Res Dev 4:15–23
13. Shen NG, Kevin C (2012) Simulations of thermo-mechanical characteristics in electron beam additive manufacturing, ASME 2012 international mechanical engineering congress & exposition. Houston, TX
14. Zaeh MF, Branner G (2010) Investigations on residual stresses and deformations in selective laser melting. Pro Enging Res Dev 4:35–45
15. Dinda GP, Dasgupta AK, Mazumder J (2009) Laser aided direct metal deposition of Inconel 625 superalloy: microstructural evolution and thermal stability. Mater Sci Eng, A 509:98–104
16. Gaumann C, Bezencon C, Canalis P, Kurz W (2001) Single crystal laser deposition of superalloys: processing—microstructure maps. Acta Mater 49:1051–1062
17. Zhao XM, Chen J, Lin X, Huang WD (2008) Study on microstructure and mechanical properties of laser rapid forming Inconel 718. Mater Sci Eng, A 478:119–124
18. Li LJ (2006) Repair of directionally solidified superalloy GTD-111 by laser-engineered net shaping. J Mater Sci 41:7886–7893
19. Moat RJ, Pinkerton AJ, Li L, Withers PJ, Preuss M (2009) Crystallographic texture and microstructure of pulsed diode laser-deposited Waspaloy. Acta Mater 57:1220–1229
20. Goldak J, Chakravarti A, Bibby M (1984) New finite element model for welding heat sources. Metall Mater Trans B 15:299–305
21. Goldak J, McDill M, Oddy A, House R, Chi X, Bibby M (1986) Computational heat transfer for weld mechanics. ASM International, Ohio pp. 15–20
22. Lindgren LE (2001) Finite element modeling and simulation of welding part 1: increased complexity. J Therm Stresses 24:141–192
23. Truman CE, Smith MC (2009) Editorial: the NeT residual stress measurement and modelling round robin on a single weld bead-on-plate specimen. Intl J Pres Ves Pip 86:1–2
24. ABAQUS Users' Manual, v.6.4 (2003) Hibbitt, Karlsson & Sorensen Inc., Providence, RI
25. William H. Cubberly et al. (1978) Properties and selection: irons and steels, ASM International, ASM Metals handbook. Vol. 1. Ohio
26. ThyssenKrupp VDM (1993) Material data sheet no. 4020 Nicrofer 5120 CoTi alloy C-263
27. Shan X, Davies CM, Wangsdan T, O'Dowd NP, Nikbin KM (2009) Thermo-mechanical modelling of a single-bead-on-plate weld using the finite element method. Intl J Pres Ves Pip 86:110–121
28. Withers PJ, Bhadeshia HKDH (2001) Residual stress part 1 - measurement techniques. Mater Sci Tech 17:355–365
29. De Freitas M, Pereira MS, Michaud H, Pantelis D (1993) Analysis of residual stresses induced by laser processing. Mater Sci Eng, A 167: 115–122
30. De Oliveira U, Ocelík V, De Hosson JTM (2006) Residual stress analysis in Co-based laser clad layers by laboratory X-rays and synchrotron diffraction techniques. Surf Coat Tech 201:533–542
31. Korsunsky AM, Wells KE, Withers PJ (1998) Mapping two-dimensional state of strain using synchrotron X-ray diffraction. Scripta Mater 39:1705–1712
32. Korsunsky AM, Baimpas N, Song X, Belnoue J, Hofmann F, Abbey B, Xie MY, Andrieux J, Buslaps T, Neo TK (2011) Strain tomography of polycrystalline zirconia dental prostheses by synchrotron X-ray diffraction. Acta Mater 59:2501–2513
33. Daymond MR, Bourke MAM, Von Dreele RB, Clausen B, Lorentzen T (1997) Use of rietveld refinement for elastic macrostrain determination and for evaluation of plastic strain history from diffraction spectra. J Appl Phys 82:1554–1562
34. Frampton L (2009) Interim report of initial mechanical test data for Direct Metal Laser Sintered (DMLS) C263 material, RR internal report, MFR47228, Issue 1